Electrochemical Properties and Nucleation Morphology of Yttrium on Tungsten Substrate in Molten Salt

Journal of The Electrochemical Society, 2020 **167** 112508
1945-7111/2020/167(11)/112508/11/$40.00 © 2020 The Electrochemical Society ("ECS"). Published on behalf of ECS by IOP Publishing Limited

Electrochemical Properties and Nucleation Morphology of Yttrium on Tungsten Substrate in Molten Salt

Kui Liu,[1] Wei Wang,[1] Yue Ma,[1] Mingliang Kang,[1,z] and Biao Wang[1,2,z]

[1]*Sino-French Institute of Nuclear Engineering and Technology, Sun Yat-sen University, Zhuhai, 519000, People's Republic of China*
[2]*School of Physics, Sun Yat-sen University, Guangzhou 510275, People's Republic of China*

In this work, the diffusion coefficient and electrocrystallization of yttrium in LiCl-KCl eutectic are typically investigated using different electrochemical techniques such as cyclic voltammetry (CV), chronopotentiometry (CP) and chronoamperometry (CA) techniques. At temperature from 673 to 823 K, the diffusion coefficients of two yttrium concentrations ($YCl_3 = 3.816 \times 10^{-5}$ and 9.981×10^{-5} mol ml^{-1}) were determined by CP and CV methods in a range from 0.453×10^{-5} to 8.25×10^{-5} cm^2 s^{-1}. The nucleation of Y electrodeposition is confirmed to be an instantaneous mode regardless the given temperature, over-potential and concentrations. The morphology of yttrium nuclei and growth evolution on a tungsten surface were characterized by the SEM-EDS. Some individual circular regions corresponding to initial Y nucleation sites are firstly observed on the tungsten surface. The subsequent formed Y nuclei were found to migrate toward those circular nucleation sites to extend its growth on the inside and peripheral of the circle. In addition, no distinct dendritic structure for the Y deposition was observed on the W surface.
 [DOI: 10.1149/1945-7111/aba7db]

Manuscript submitted March 20, 2020; revised manuscript received July 13, 2020. Published July 29, 2020.

The partitioning and transmutation of spent nuclear fuel (SNF, 96% uranium, 1% Plutonium, 0.1% minor actinide and 3% fission products) for the purpose of regenerating power,[1] has been an ultimate objective of reliable and sustainable fuel cycle since the dawn of the nuclear fission energy. Since last decades, pyrometallurgical reprocessing of spent fuel is considered to be the most promising option compared to conventional hydrometallurgical processing.[2] Owing to the radiation resistance of molten salts, the absence of neutrons absorption, low physical volume, and resistance to proliferation, the pyroprocessing technology based on molten salts (such as LiCl-KCl eutectic) has being widely investigated in order to fulfill the final practical application.[3] Rare earth (RE) elements are known as the neutron poisons taking on the quarter fission products of the SNF.[4] Thus, the separation and extraction of the RE elements plays a crucial role in the pyroreprocessing of SNF.

Yttrium is one of the rare earth elements occupying 529 milligrams per kilogram of uranium in the SNF arising from typical light water reactor fuel irradiated to 40000 MWd/ton.[5] In addition, it is also widely used as an alloying element in some functional materials. For example, Y alloys are widely used in automotive, aerospace and aviation industry, and they are also excellent hydrogen storage materials due to their considerably low density and high tensile strength.[6] In addition, during the operation of electrorefining process, RE elements can be accumulated in a molten chloride salt.[7] In this case, the electrochemical method applied in the high temperature melts is unique not only for salt purification and recycling but also for RE extraction in the electrorefining process. Thus, it is of great significance to well understand the yttrium electrochemistry in molten salt.

In 1959, the equilibrium electrode potentials of Y^{3+}/Y couple were verified in the LiCl-KCl eutectic by Yang and Hudson.[8] Later in 1970, for the specific motivation of electrochemical separation of fission product impurities, HOSHIN et al. studied the electrochemical and thermodynamic properties of yttrium and yttrium-zinc alloys in fused LiCl-KC1 eutectic.[9] Since then, many works were conducted to extend the yttrium electrochemistry in chloride molten salts, such as the electrochemical behaviors on different electrodes such as Ni,[10–13] Cu,[14] Mo[12] and W,[2,13] co-reduction mechanisms with other cations,[6,15,16] investigations of cathodic kinetics, diffusion coefficient and electrocrystallization mechanism.[2] Castrillejo et al. found that the nucleation mechanism of yttrium deposition on the tungsten electrode is an instantaneous nucleation process in the eutectic LiCl-KCl.[2] However, available studies for yttrium are still limited especially relating to kinetic properties and electrocrystallization phenomena. Typically, no existing data has been recorded for the visualization of early stage nucleation and growth of yttrium electrodeposition in molten salt.

In this work, the kinetic parameters of diffusion coefficient and electrocrystallization of yttrium are specifically investigated in the LiCl-KCl eutectic. Particularly, an inert tungsten disk electrode was used to achieve the SEM characterization of Y electrodeposits. The initial stage of morphologies for Y nucleation and growth on tungsten substrate are documented by SEM micrographs. The results can help us better understand the yttrium molten salt electrochemistry and provide some fundamental data for the preparation of yttrium materials and for the RE separation and extraction in pyroprocessing process.

Experimental

Chemicals and melt preparation.—The LiCl-KCl eutectic (51:49 mol%) was directly prepared by anhydrous lithium chloride (>99.0%) and potassium chloride (>99.5%) (Aladdin, Shanghai). First, the LiCl-KCl mixture was introduced into a vitreous carbon crucible and placed in a vacuum drying oven at 473 K for more than 24 h in order to remove as much free water as possible from commercial salts. Subsequently, the anhydrous mixture was transferred into the glove box and introduced into the vitreous carbon crucible placed in the resistance furnace, which was heated to 873 K in an argon atmosphere. This was maintained for 24 h or more, then naturally cooled to room temperature. After cooling to room temperature, the solid salt ingot was easily removed from the vitreous carbon crucible and some black impurities on the salt surface were scraped off using a mini bench grinder. This procedure was repeated triple times in order to remove as much of residual water and impurities as possible from the eutectic. After that, we obtained a relatively pure salt ingot for the experiment, smashed it, and stored it in a jar in the glove box for later use. In the electrochemical test, yttrium chloride (99.9%, Alfa Aesar) was directly introduced into the molten LiCl-KCl eutectic. The actual concentration of yttrium ions in the melt was determined by an inductively coupled plasma optical emission spectrometer (ICP-OES, Agilent 5110).

Apparatus and electrodes.—The chemical storage, handling of molten salt and electrochemical experiments were all carried out in a glove box (Wigor, HG1500/750TS) with a pure argon atmosphere (99.999% Ar, H_2O < 0.5 ppm, O_2 < 1 ppm). A programmable

[z]E-mail: kangml3@mail.sysu.edu.cn; wangbiao@mail.sysu.edu.cn

electric furnace (Jiuchen, GR2–270) with a stainless steel (ϕ64 × 150 mm) and corundum crucible (ϕ50 × 100 mm) inside was placed in the glove box. The furnace maintained the temperature with an accuracy of ±1 °C. An Omega thermometer (HH806AU) was used to measure the actual temperature of the melt system. An electrochemical workstation (Gamry 3000 Reference) was used to apply voltage or current for electrochemical measurements.

The scheme of the electrochemical cell has been described in our previous work.[17] Two kinds of working electrodes were applied. One is the widely used tungsten wire (ϕ = 1 mm) cathode, and another is a tungsten disk (9 mm D × 1 mm l) electrode encapsulated by a cylinder boron nitride (BN) shroud which is made up of a fastening screw rod and a lock nut.[18] The disk inside is clamped between the BN lock nut and a stainless steel (SS) cylinder connecting a SS wire sealing in the BN screw rod as current collector. At the end of the lock nut, a small hole (2–5 mm) was previously drilled in order to contact and conduct with the melt. Both the upper and lower surfaces of the W disk was carefully polished (2000 and 3000 mesh sand paper, 1.2 micron SiC and 1.0 micron and 0.05 micron Al_2O_3 were used in succession) to a mirror like condition. Carbon rod (ϕ = 4 mm) was used as a counter electrode. Tungsten wire and carbon rod were polished by emery papers and then cleaned by diluted hydrochloric acid, ultrapure water and alcohol prior to the experiments. For a reference electrode, an alundum tube containing a silver wire (ϕ = 0.5 mm) was used, which was filled with LiCl-KCl-(1 wt%) AgCl salt. The bottom of the corundum tube was polished by a sander to provide a very thin diaphragm which can promote ionic conduction in the high temperature molten melt.

Electrochemical techniques and sample characterization.— Three different electrochemical techniques, cyclic voltammetry (CV), chronopotentiometry (CP) and chronoamperometry (CA), were employed to study the electrochemical redox reactions of YCl_3 in LiCl-KCl eutectic from 673 K to 823 K. To guarantee the consistency and reproducibility of the electrochemical test at each temperature, each of these electrochemical techniques was programmed several times by Gamry workstation software. All the electrochemical data were analyzed by Matlab R2019b. For the electrodeposition of yttrium sample, potentiostatic electrolysis was carried out on the tungsten disk electrode at different overpotential at 773 K. After deposition, the cooled tungsten disk can be readily detached. Its mirror-like surface enabled the solid salt in the hole at the end side of the BN lock nut to be easily stripped off and only kept the yttrium deposits staying without adhering too much salt. To characterize the surface morphology and composition of the deposits, the detached disk was firstly adhered on a copper sample stage by using conducting resin in a glove box and placed in an airtight canister. Then, the airtight canister was transferred to the scanning electron microscopy (SEM)-energy dispersive X-ray (EDX) (Quanta 400 FEG) at ambient humidity <30%RH. After open the canister, the copper stage was rapidly placed in the vacuum chamber within 5 s to avoid the oxidation of initial yttrium deposits as much as possible.

Results and Discussion

Electrochemical properties of yttrium in LiCl-KCl eutectic.— The electrochemical behaviors, diffusion coefficients and apparent standard potentials of yttrium in LiCl-KCl eutectic were studied by cyclic voltammetry (CV), chronopotentiometry (CP) and open circuit potential (OCP) at different temperatures ranging from 673 to 823 K.

Figure 1a presents the comparison of the cyclic voltammograms recorded in the blank LiCl–KCl eutectic (blue curve) and in the LiCl–KCl-(3.816 × 10^{-5} mol ml^{-1}) YCl_3 melt (orange curve) recorded on a tungsten wire electrode at 723 K. The baseline (blue curve) of LiCl-KCl eutectic shows only the current responses of the reduction of Li^+ and the release of Cl_2 at ∼−2.407 and ∼1.26 V, respectively. The orange curve illustrates a sharp redox couple with cathodic peak at approximately −2.08 V and it associated anodic peak at −1.884 V, indicating the feature of a formation and dissolution of a new solid phase on the surface of the electrode. The inset in Fig. 1a shows more details about the baseline, and the current response of the blank eutectic at the reduction potential range of Y^{3+} is ∼−0.001 A, which even became smaller after the introduction of YCl_3 and serval hours of melt homogeneous equilibrium process. This phenomenon suggests that the influence of baseline on Y reductive current response is limited. It has been proved that the reduction of yttrium is a one-step reaction in the Refs. 2, 9. Figure 1b shows a series of CV curves for Y^{3+} recorded on a tungsten wire electrode in the LiCl-KCl-(9.981 × 10^{-5} mol ml^{-1}) YCl_3 melts with different scan rates after the correction of IR drop. These typical voltammograms of Y^{3+}/Y^0 redox system demonstrate that the potentials of redox peak primarily remain the same level regardless of the variation of the scan rate. Therefore, the reaction of Y^{3+}/Y^0 can be considered as a reversible reaction.

For a soluble-insoluble reversible couple system, the diffusion coefficient D of Y^{3+} in the melt can be deduced by employing the Berzins–Delahay equation,[19]

$$\frac{I_p}{\sqrt{v}} = 0.61\frac{(nF)^{3/2}}{\sqrt{RT}} S C_{Y^{3+}} \sqrt{D_{Y^{3+}}} \qquad [1]$$

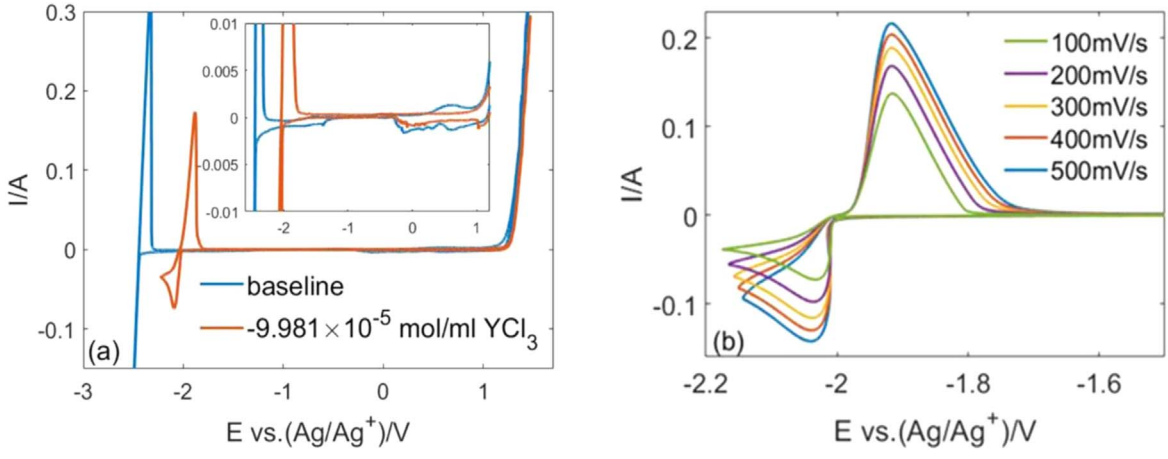

Figure 1. (a) Comparison of the cyclic voltammograms recorded in the blank melt and the LiCl–KCl-(9.981 × 10^{-5} mol ml^{-1}) YCl_3 melt recoding at 100 mV s^{-1}, (b) Scan rates dependence of cyclic voltammograms on tungsten wire electrode, S = 0.479 cm^2.

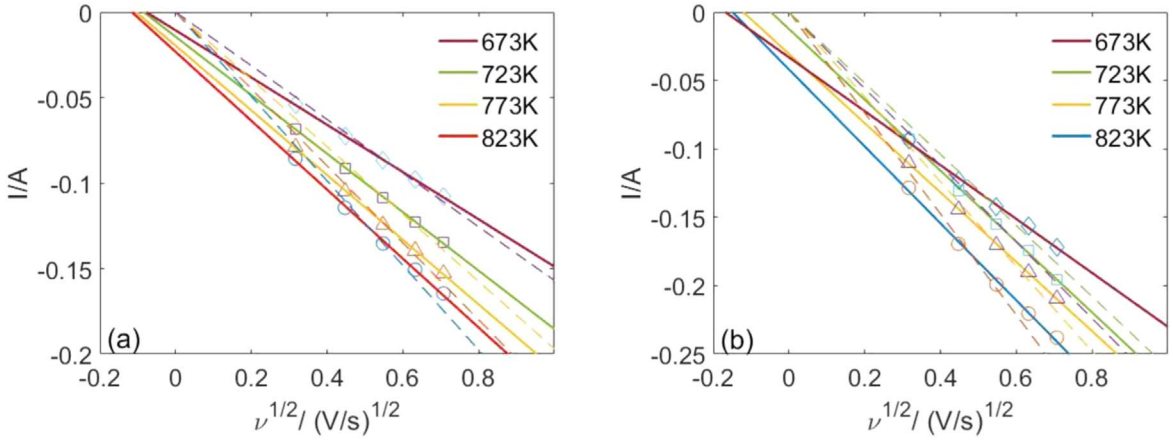

Figure 2. The linear relationships between I and the square root of the scan rate at different temperatures with (a)$YCl_3 = 3.816 \times 10^{-5}$ mol ml^{-1}, $S^{-1} = 0.4475$ cm^2 and (b) $YCl_3 = 9.981 \times 10^{-5}$ mol ml^{-1}, $S^{-1} = 0.479$ cm^2.

where I_p is the peak current of cathodic wave in Fig. 1, υ is the scan rate in V s^{-1}, n is the number of electrons transferred, F is Faraday's constant, C_Y^{3+} is the more concentration of Y^{3+}, S is the surface area of the working electrode, n is the number of exchanged electrons and D is the diffusion coefficient of Y^{3+} for different temperatures (T, 673 $\sim$ 823 K).

Figures 2a and 2b present the linear relationships between peak current and square root of scan rate fitted by the Berzins–Delahay equation (dash line) and actual experimental trend (line) at different temperatures (from 673 to 823 K). In fact, the practical experimental trend does not strictly pass the zero point to match the Berzins–Delahay equation. One possible reason is the influence of Y nucleation on the W surface in the high temperature molten salt which highly affected the current response. It is reasonable and understandable for the experimental data and the theoretical mode to have some discrepancies since the Berzins–Delahay equation was established and verified based on the data primarily collected in aqueous solution.[19] This discrepancy was also found in many published works involving molten salt system, although all these works have been trying to fit a zero-passed linear relationship.[20–24] Nevertheless, the dash line represents the calculated the diffusion coefficient of Y^{3+} for a comparison with the one deduced by CP method and those in literature as shown in Table I and Fig. 5.

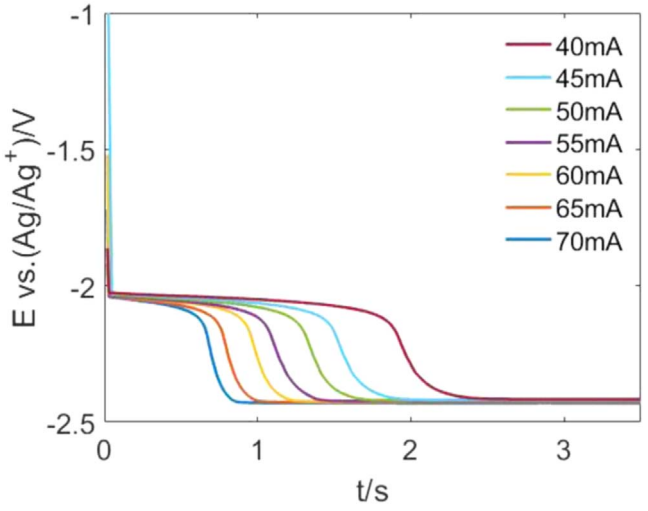

Figure 3. CP curves of yttrium collected on tungsten wire electrode in molten LiCl-KCl-YCl_3 (9.981×10^{-5} mol ml^{-1}) at 773 K with different applied current, S = 0.479 cm^2.

Figure 3 illustrates the CP curves for YCl_3 (9.981×10^{-5} mol ml^{-1}) recorded on a tungsten wire electrode in LiCl-KCl eutectic melts at 773 K at different applied currents. Under all current conditions from 40 to 70 mA, potential platforms for Y^{3+}/Y^0 always maintain at the same level regardless of current applied. This phenomenon suggests the possible reversible of Y^{3+}/Y electrode reaction. Therefore, the reversibility of the Y^{3+}/Y^0 and the linear relationship between I and $\tau^{-1/2}$ (Figs. 4a and 4b) guarantees the application of the Sand's law[25]:

$$I\sqrt{\tau} = 0.5nFC_{Y^{3+}}S\sqrt{\pi D_{Y^{3+}}} \quad [2]$$

where τ is the transition time in seconds.

With the aid of these two formulas, the diffusion coefficients of Y^{3+} can be deduced by CV and CP methods. Tests were repeated several times under the same condition at each temperature and concentration. The average results are summarized in Table I.

In our work, the diffusion coefficients calculated by two different electrochemical at the same temperature are slightly different (CP > CV). However, all the linear lines (log D vs 1/T) demonstrate a similar slope relating to the activation energy in the melt, which will be explained later. This phenomenon infers the validity and rationality of our experiment. In addition, whether the value is large or not, the principal reason for the diversity is ascribed to the difference of methodology as mentioned. Castrillejo et al. found that the diffusion coefficient of Y^{3+}(1.095×10^{-5}mol cm^{-3}) at tungsten electrode is approximately equal to 1.00×10^{-5} cm^{2}s^{-1} by using a semi-integral CV and 0.93×10^{-5} cm^{2}s^{-1} by the chronopotentiometry, respectively, in eutectic LiCl-KCl molten salts at 723 K[2]. F. Lantelme et al. obtained that the diffusion coefficient D equals to 6.5×10^{-6} cm^{2}s^{-1} in LiCl-KCl at 750 K.[13] In the work by Jiwen He et al., the diffusion coefficient D of yttrium in molten eutectic NaCl-KCl at 973 K is 2.8×10^{-5} cm^{2}s^{-1} by employing the CV method.[6]

Table I. Diffusion coefficients (10^5D, cm^2 s^{-1}) of Y^{3+} in LiCl-KCl-YCl_3 melts (YCl_3, $C_1 = 3.816 \times 10^{-5}$ mol ml^{-1}, $C_3 = 9.981 \times 10^{-5}$ mol ml^{-1}) at different temperatures.

	CP		CV	
T(K)	C_1	C_3	C_1	C_3
673	4.81	1.55	0.676	0.453
723	5.96	1.79	1.14	0.565
773	7.10	2.19	1.59	0.740
823	8.25	2.58	2.05	1.12

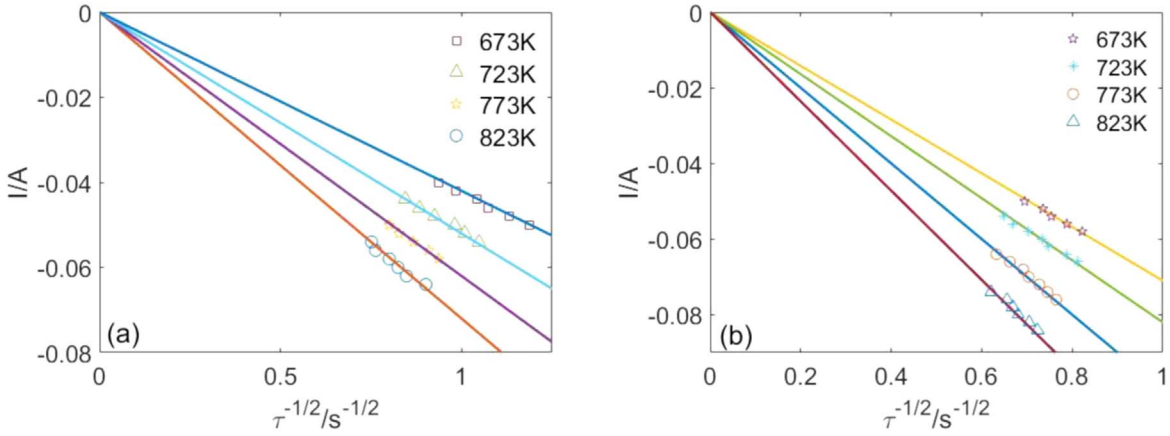

Figure 4. The linear relationships of I vs $\tau^{-1/2}$ for the chronopotentiometric data obtained in LiCl-KCl eutectic, (a)$YCl_3 = 3.816 \times 10^{-5}$ mol ml^{-1}, $S^{-1} = 0.4475$ cm^2 and (b) $YCl_3 = 9.981 \times 10^{-5}$ mol ml^{-1}, $S^{-1} = 0.479$ cm^2.

Compared with the results in this work, the subtle differences are probably caused by different conditions in the experiments, such as temperatures, methods applied, molten salts system and so on. In addition, the possible presence of some additional contributions, such as concurrent electrochemical processes, convection, nucleation, dendritic growth etc, may also have an impact on the determination of diffusion coefficient.

In Fig. 5, the linear relationships between log D and T^{-1} are fitted as Eqs. 3–6 for Y^{3+} in the molten salt and compared them with that in literature. The comparable slopes between these lines in Fig. 4 guarantee the validity of these data.

In the CV experiments:

$$C_1 \log D_{Y^{3+}} = -2.79 - \frac{1771}{T} \quad [3]$$

$$C_3 \log D_{Y^{3+}} = -3.537 - \frac{1415}{T} \quad [4]$$

In the CP experiments:

$$C_1 \log D_{Y^{3+}} = -3.00 - \frac{891}{T} \quad [5]$$

$$C_3 \log D_{Y^{3+}} = -3.587 - \frac{829}{T} \quad [6]$$

Through these linear relationships (L1-L6) fitted in the Fig. 5, the validation of the Arrhenius law can be verified in our systems as follows,

$$D = D^0 e^{-\frac{E_a}{RT}} \quad [7]$$

where D^0 is the pre-exponential factor, E_a presents the activation energy (kJ mol^{-1}), and T is the absolute temperature of K. The apparent activation energies can be calculated by applying the relationship of temperature and diffusion coefficient in Table I. The calculated results for $YCl_3 = 3.816 \times 10^{-5}$ mol ml^{-1} are 17.06 and 33.90 kJ mol^{-1} for CP and CV, respectively. For $YCl_3 = 9.981 \times 10^{-5}$ mol ml^{-1}, the corresponding values are 15.87 and 27.09 kJ mol^{-1}, respectively. These results are comparable to the data of 31.94 kJ mol^{-1} reported in the literature[2].

By using the open circuit potential (OCP) techniques, the equilibrium potential and the apparent standard potential of Y^{3+}/Y can be calculated. In Fig. 6, at each studied temperature, an obvious stable plateau was obtained relating to the corresponding pseudo-equilibrium potential $E^{eq}_{Y^{3+}/Y}$ and the apparent standard potential $E^{*}_{Y^{3+}/Y}$ by the Nernst relationship, as follows:

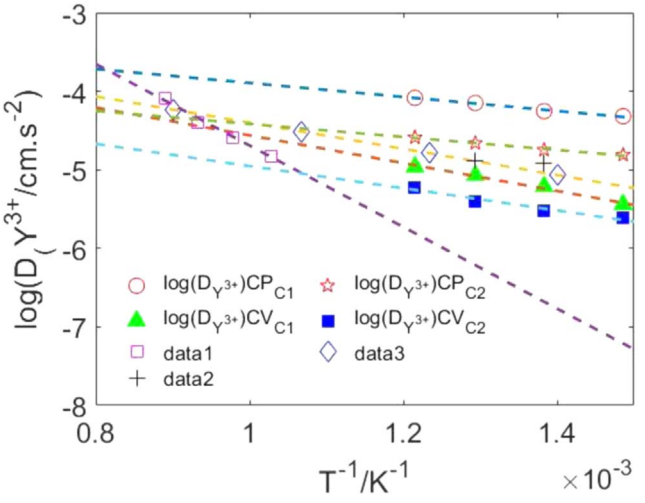

Figure 5. The linear relationships between log D and 1/T for Y^{3+}(with $C_1 = 3.816 \times 10^{-5}$ mol ml^{-1} and $C_3 = 9.981 \times 10^{-5}$ mol ml^{-1}) determined respectively by CP (○ and ☆) and CV(▲ and ■) in this work. Comparison of values in literature, ◇ LiCl-KCl[2], □NaCl-KCl,[14] + LiCl-KCl.[26]

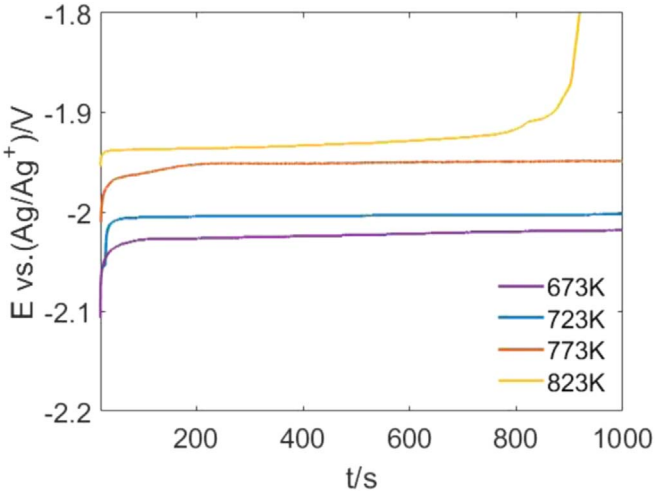

Figure 6. Typical OCP curves recorded in LiCl-KCl-YCl_3 = 1.8 wt% at different temperatures.

$$E^{eq}_{Y^{3+}/Y} = E^{0}_{Y^{3+}/Y} + \frac{RT}{nF}\ln\left(\frac{a_{Y^{3+}}}{a_Y}\right) \quad [8]$$

$$E^{*}_{Y^{3+}/Y} = E^{0}_{Y^{3+}/Y} + \frac{RT}{nF}\ln\left(\gamma_{Y^{3+}}\right) \quad [9]$$

where $E^{0}_{Y^{3+}/Y}$ represents the standard potential at a hypothetical supercooled liquid reference of unit mole fraction and unit activity, $a_{Y^{3+}}$ and a_Y are the activity of Y^{3+} ions and the metallic Y. $\gamma_{Y^{3+}} = \frac{a_{Y^{3+}}}{x_{Y^{3+}}}$ represents the activity coefficient of Y^{3+} and $x_{Y^{3+}}$ is the mole fraction of Y^{3+} in the melt. The activity of pure metal is assumed 1 by default.

To better compare these potentials with those in literature, the potentials mentioned above was recalculated vs Cl_2/Cl^- reference electrode according to the following equation:

$$E_{Ag/AgCl}(\text{vs}\ (Cl_2/Cl^-)) = E^{0}_{AgCl} + \frac{RT}{nF}\ln\ X_{AgCl} \quad [10]$$

In the work of Yang et al.,[8] the data obtained at a low AgCl concentration is extrapolated to infinite dilution. Subsequently, the potential of reference electrode employed in this work (0.0039 mole fraction AgCl) vs Cl_2/Cl^- is given by the following equation:

$$E_{Ag/AgCl}(\text{vs}\ (Cl_2/Cl^-)) = -1.0910 - 1.855 \times 10^{-4}T(K) \quad [11]$$

Based on Eqs. 8–10, $E^{eq}_{Y^{3+}/Y}$ can be expressed as:

$$E^{*}_{Y^{3+}/Y}(\text{vs}\ Cl_2/Cl^-) = E^{eq}_{Y^{3+}/Y} - \frac{RT}{nF}\ln\left(x_{Y^{3+}}\right) + E_{Ag/AgCl} \times (\text{vs}\ Cl_2/Cl^-) \quad [12]$$

Using Eqs. 8–12, the values of the apparent standard potential and the equilibrium potential at different temperatures with two concentrations were calculated and summarized in Table II. Therefore, the relationships between temperature and apparent standard potential of Y^{3+}/Y are fitted in Fig. 7 as the following equations for 5.642×10^{-5} mol ml^{-1} and 9.981×10^{-5} mol ml^{-1} of YCl_3 in the melt, respectively, and these results were compared with those data calculated in different references.

$$C_2\ E^{*}_{Y^{3+}/Y}(\text{vs}(Cl_2/Cl^-)/V) = -3.56 + 5.87 \times 10^{-4}T(K) \quad [13]$$

$$C_3\ E^{*}_{Y^{3+}/Y}(\text{vs}(Cl_2/Cl^-)/V) = -3.477 + 5 \times 10^{-4}T(K) \quad [14]$$

In Fig. 7, values of apparent standard potential derived from others' works are compared with ours in LiCl-KCl eutectic. Except data 4, the literature is very close to the values in this work.

Nucleation mechanism of yttrium electrodeposition.—To further study the nucleation and initial growth of yttrium on the tungsten electrode, the fundamental method—chronoamperometry was applied. Moreover, the application of corresponding dimensionless theoretical

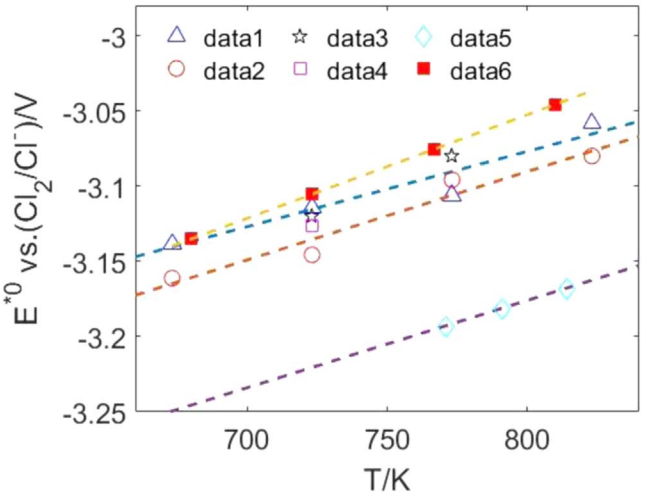

Figure 7. The temperature dependence of apparent standard potential E^{*0} of Y^{3+} vs Cl_2/Cl^- reference. △ data1 and ○ data2 are the values obtained in this work, ☆ data3-LiCl-KCl,[26] □ data4 liCl-KCl[27] and ◇ data5 liCl-KCl[8], ■ data6 liCl-KCl,[28] The dotted lines are corresponding fitted relationship.

equation can deduce typical modes for Y nuclei formation and growth. Before each CA test, two equilibrium conditions were carried out on the cell system to guarantee the consistency and reproducibility of data collection. First, a CV curve covering the redox potential of Y^{3+} and Cl^- was applied to the system with the starting and ending potentials of 0 vs Ag/AgCl. Then, a potentiostatic electrolysis was done at 0 vs Ag/AgCl for 30 s for further electrode cleaning and system equilibrium. Finally, the CA test was performed at an initial applied potential which was little more anodic than the reduction potential of Y^{3+} based on the Y concentration, covering the reductive peak potential range of Y^{3+} with a step potential of 0.005 V.

Figure 8 plots a series of typical CA curves at 773 K at different over-potentials on W wire electrode in LiCl-KCl-9.981×10^{-5} mol ml^{-1} YCl_3 melts. In this plot, two distinct current evolutions can be clearly observed. The first one is a gradual rise of current to reach a maximum value (peak, I_m) because of the formation and subsequent growth of yttrium crystals resulting from the increase in active cathodic surface. The second one is that the current follows a typical $t^{-1/2}$ decay as in the Cottrell equation, which is controlled by the mass transfer process of Y^{3+}.

Scharifker and Hills[29, 30] proposed two dimensionless theoretical modes (S-H mode) based on a 3D nucleation and growth process which are controlled by diffusion of electroactive species. The nucleation mode of the electrodeposition can be distinguished by applying this theory. The mathematical models are expressed in two cases as follows:

(I) Instantaneous nucleation which means all the yttrium nuclei are generated at the beginning of electrolysis at the same time and grew over the time;

Table II. Summary of the equilibrium potentials and the apparent standard potentials of Y^{3+}/Y in LiCl-KCl-YCl_3 melts (YCl_3, $C_2 = 5.642 \times 10^{-5}$ mol ml^{-1}, $C_3 = 9.981 \times 10^{-5}$ mol ml^{-1}) at different temperatures.

	E^{eq} vs (Ag/AgCl)/V		E^{*0}vs (Ag/AgCl)/V		E^{*0}vs (Cl_2/Cl^-)/V	
T(K)	C_2	C_3	C_2	C_3	C_2	C_3
673	−2.023	−1.988	−1.853	−1.829	−3.161	−3.139
723	−2.005	−1.960	−1.822	−1.790	−3.146	−3.114
773	−1.951	−1.943	−1.756	−1.760	−3.096	−3.106
823	−1.932	−1.897	−1.724	−1.703	−3.080	−3.058

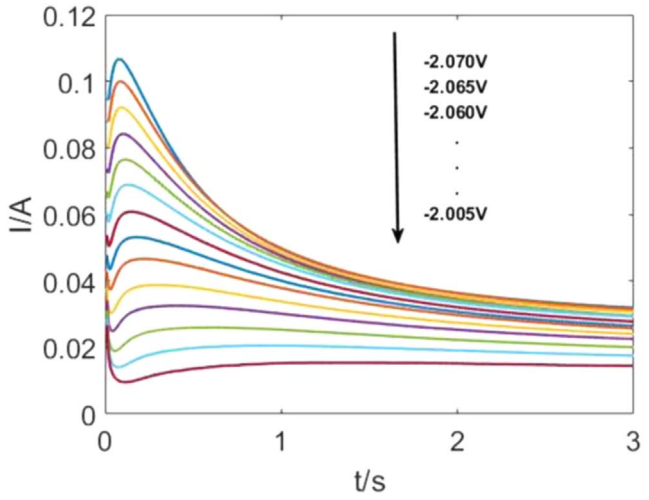

Figure 8. A series of CA curves at 773 K ranging from −2.005 to −2.070 V collected in LiCl-KCl-9.981 × 10^{-5} mol ml^{-1} YCl_3.

$$\left(\frac{I_m}{I}\right)^2 = \frac{1.97542}{\frac{t}{t_m}}\left[1 - \exp\left(-1.2564\frac{t}{t_m}\right)\right]^2 \quad [15]$$

(II) Progressive nucleation which indicates new yttrium nuclei are consecutively created throughout electrolysis;

$$\left(\frac{I_m}{I}\right)^2 = \frac{1.2254}{\frac{t}{t_m}}\left[1 - \exp\left(-2.3367\left(\frac{t}{t_m}\right)^2\right)\right]^2 \quad [16]$$

Where I_m and t_m represent the maximum of transient current and time, respectively, which can be determined by Fig. 8 directly, t is the recorded time, and j the transient current density.

In Figs. 9a and 9b, the experimental CA curves are re-plotted in $\left(\frac{I_m}{I}\right)^2$ vs $\frac{t_m}{t}$ relation for different overpotentials and temperatures, respectively, and compared with the dashed curve 1 and dotted curve 2 form the theoretical models described by Eqs. 15 and 16. In Fig. 9, the experimental data implies a tendency in terms of the dimensionless theoretical model (dashed curve 1) for instantaneous nucleation with 3D growth of the nuclei at all studied concentrations, overpotentials and temperatures. Accordingly, yttrium nuclei are generated at the same time on all active sites available at the initial stage of electrolysis. Castrillejo et al. also suggested that the nucleation of yttrium on tungsten is an instantaneous mode.[2] In addition, Fig. 9 also suggests that the studied range of Y concentrations, temperatures and overpotential have a limited effect on the nucleation mechanism. It should be mentioned that the experimental data cannot meet a good fitting to the instantaneous mode. The data published in many works[3,17,31–33] also present this discrepancy. One possible reason might be the different experimental protocols such as different electrodes, cell configurations, data collection and processing, etc. Moreover, it should be mentioned that the Eqs. 15 and 16 were derived for a specific and simple situation: the diffusion controlled three-dimensional nucleation of electroactive species with fast electron transfer kinetics, in the absence of any other contributing process. The fast electron transfer kinetics in the high molten salt system is very easy to figure out. It is found that in the high temperature molten salt system, a severe adsorption behavior was found on the electrode surface accompanied with a metal electrochemical reduction process, which highly affected the potential and current response.[34–36] Recent works[3,31] attempted to explain this discrepancy, they found that even though the S-H mode suggests a 3D nuclei formation, the SEM images of initial nuclei morphology presents a 2D growth. Similar phenomenon is also observed in our work which will be discussed in the next section. In addition, some researchers are trying to establish a nucleation mode considering the adsorption behavior in the high temperature molten salt system.[35] It is quite clear that more works need to be done to get a good understanding on this issue.

Morphology evolution of yttrium electrodeposition.—As mentioned before, the initial stage of yttrium nucleation and following growth can be predicated by applying theoretical electrochemical models of (15) and (16) to fit CA curves. However, the visual information of nucleus morphology and growth evolution, which are very important for understanding the subsequent deposition, are still needed to confirm the mode.

It is a challenge to obtain the early stage of nuclei samples in molten salt electrodeposition. The early nuclei generally are deposited during a very short time; therefore, the sample quantity is minimal. More troublesome, micro-sized nucleus samples are very sensitive to water and oxygen, especially to those active elements such as lanthanides, and generally attach larger amount of solid salts after electrodeposition. Thus, it is problematic to be obtain the initial nuclei by solvent cleaning. In the references, Tang and Pesic given a

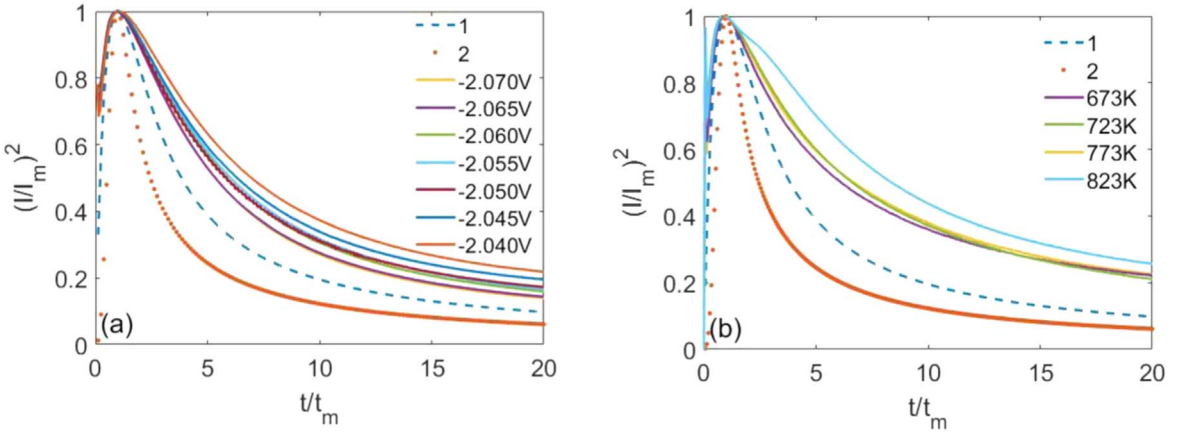

Figure 9. A comparison of the dimensionless experimental data with the theoretical models of progressive (dotted curve 2) and instantaneous (dash curve1) nucleation at (a) different overpotentials at 773 K in LiCl-KCl-9.981 × 10^{-5} mol ml^{-1} YCl_3 and (b) different temperatures with 100 mV overpotential vs $E^{eq}_{Y^{3+}/Y}$ in LiCl-KCl-3.816 × 10^{-5} mol ml^{-1} YCl_3.

straightforward and smart idea to prepare a Mo disk electrode from a side-shielded 3 mm D × 10 mm l Mo cylinder.[31] After carefully polished its open end, they found that the freshly and well-polished surface of Mo did not retain molten salt upon its withdrawal. As a result, they obtained high-quality SEM images for initial nuclei formation and growth of several lanthanides elements in molten salt electrolysis.[3,31–37] However, due to the thick size and complex shielding of the Mo cylinder electrode, we need to design a special sample stage for the electron microscope. It is inconvenient in the process of sample preparation for SEM analysis. In addition, tungsten material, owing to its strong chemical stability and corrosion resistance performance in high temperature molten salt, has been widely used as cathode in molten salt electrochemical study. If we can obtain the initial nuclei morphology on the tungsten surface, it would be very helpful to better understand the yttrium electrochemistry. The tungsten disk (9 mm D × 1 mm l) electrode used in this study can readily solve these problems mentioned above.

By employing the tungsten disk electrode and scanning electron microscopy, the first few seconds of yttrium nucleation and growth can be visualized. Figure 10 presents the SEM images of tungsten disk electrode surface after electrodeposition of Y at −2.07 V vs Ag/AgCl in LiCl-KCl-9.981 × 10^{-5} mol ml^{-1} YCl_3 or 3.816 × 10^{-5} mol ml^{-1} YCl_3 melts at 773 K at 2 s and 5 s, respectively. Some individual circular regions range from dozens to hundreds of microns (Figs. 10a–10b) corresponding to the Y nucleation sites can be visualized on the tungsten surface. According to the previous study on Mo surface for Nd and Er deposition,[3,37] this phenomenon is a typical characteristic for the case of instantaneous nucleation, where the nuclei are typically concentrated at the center and the following centrifugal diverging growth arranged to form lower density of dendrites. Even though our case firstly focused on the Y nucleation morphology on W surface, the emergence of some individual circular regions can still inspire our understanding in the Y nucleation. However, the mechanical or physical state after polishing, the magnetic field during the electrodeposition and the possible micro gas bubbles on the W surface after introduced in molten salt may also the possible reasons to cause such large cycles up to hundreds of microns.

Nevertheless, there are still some distinctive information for the yttrium nucleation on W surface. Here, high density nuclei seem gathered at the circular area and the sequential arrangement grown both at the peripheral and center-orientated directions. The obvious discrepancy is that no visible dendritic morphology is observed for Y deposition on the W surface, but circular chains arrangement clearly appears in the backscattered SEM images for the following growth (Figs. 10c–10d). It is believed that Y nuclei

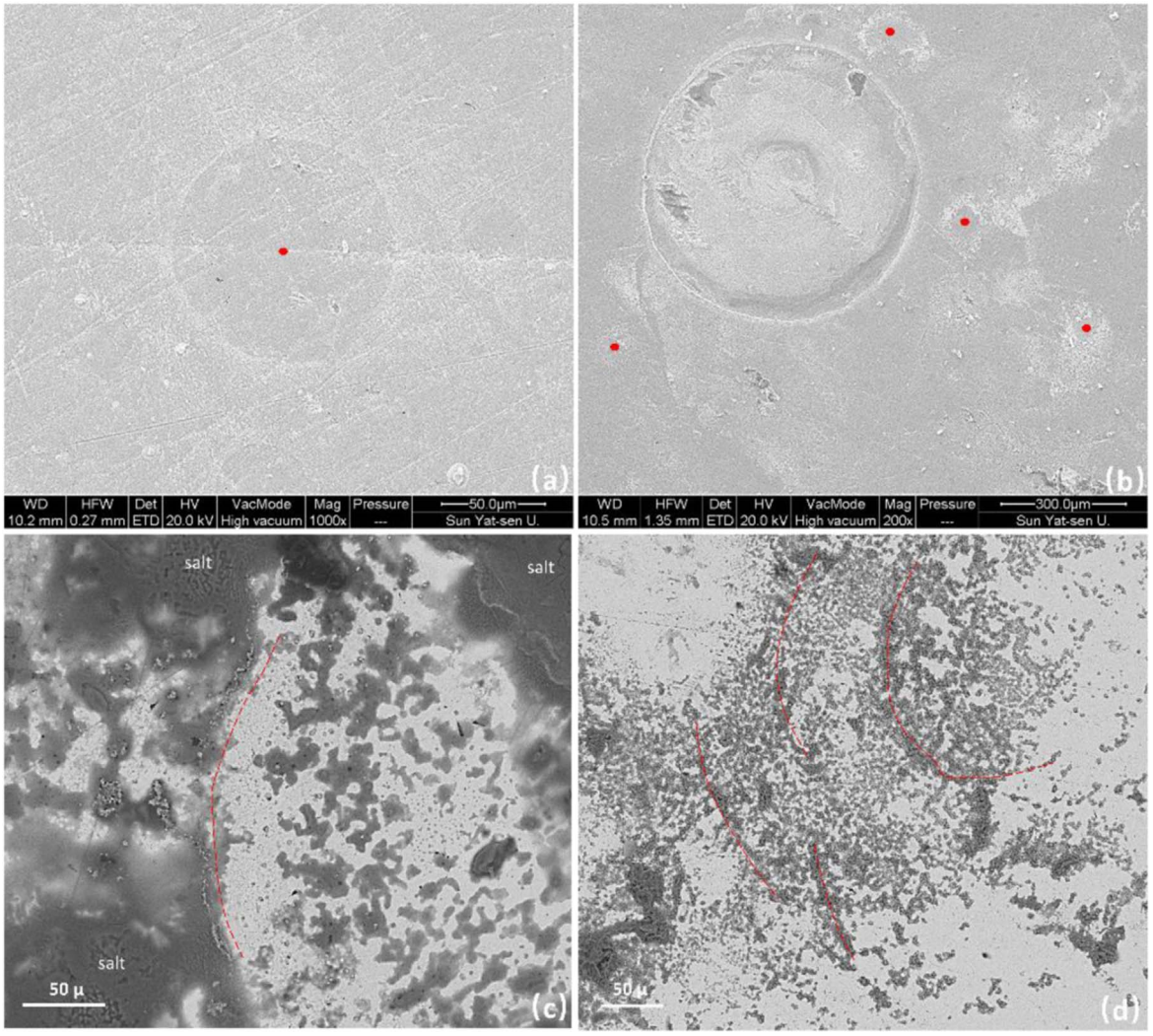

Figure 10. SEM images of tungsten disk electrode surface after electrodeposition of Y at −2.07 V vs Ag/AgCl in LiCl-KCl-9.981 × 10^{-5} mol ml^{-1} YCl_3 melts at 773 K. deposition time, (a) 2 s, (b) 5 s, (d) 10 s and LiCl-KCl-3.816 × 10^{-5} mol ml^{-1} YCl_3 melts, (c) 5 s, (c),(d) backscattered image.

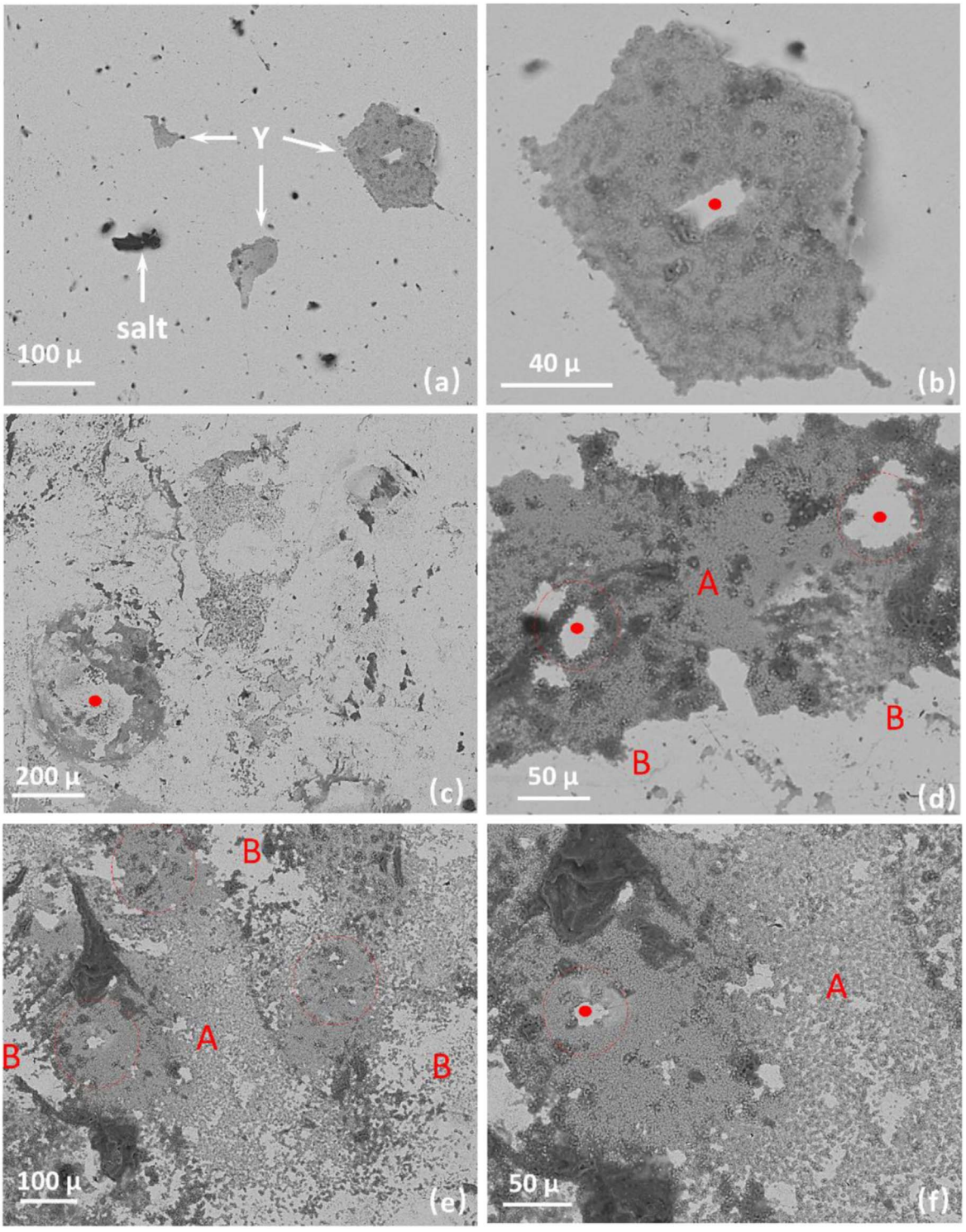

Figure 11. SEM images (backscattered) of tungsten disk electrode surface after electrodeposition of Y at −2.07 V vs Ag/AgCl inLiCl-KCl-9.981 × 10^{-5} mol ml^{-1} YCl_3 melts at 773 K. deposition time, (a)–(b) 5 s, (c)–(d) 10 s, (e)–(f) 30 s.

are highly mobile on the W surface during the deposition. Once a circular chain initially forms, the nuclei instantaneously form somewhere on the W surface, and migrate toward the circular nucleation sites to promote the following growth inside and at the peripheral of the circle. This explanation is supported by the observation in Fig. 11.

On the same sample with Fig. 10b for 5 s of electrodeposition, a very compact and center-empty pentagonal area for Y film is also presented in the SEM images as shown in Figs. 11a–11b. This hollow compact film structure appears more in the following samples for a longer time of deposition. In Figs. 11c–11f for the 10 s and 20 s of deposition, several individual compact areas

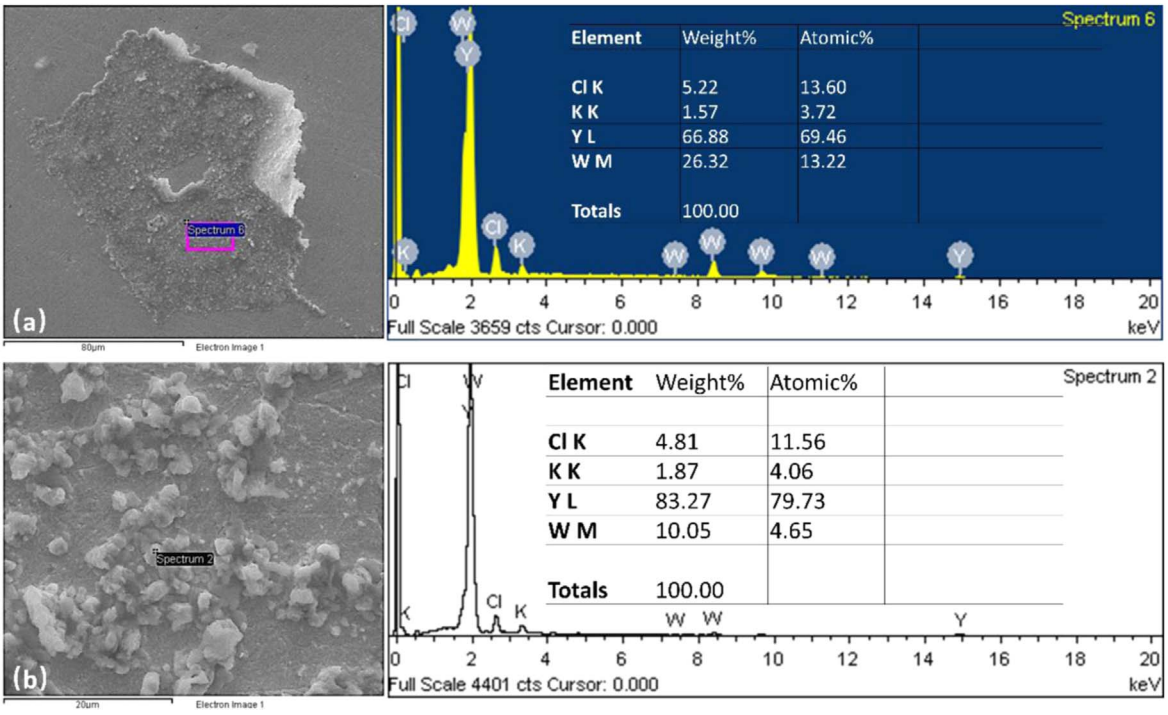

Figure 12. SEM images and EDS analysis of tungsten disk electrode surface after electrodeposition of Y at −2.07 V vs Ag/AgCl inLiCl-KCl-9.981 × 10^{-5} mol ml^{-1} YCl_3 melts at 773 K. deposition time, (a) 5 s, (b) 10 s.

(red dotted cycle) with their hollow centers (red point) and low-density peripheries can be observed, presenting a high coverage rate of Y deposits. The corresponding EDS analyses are presented in Fig. 12. Even though the signals of chlorine and potassium appear due to the impossibility of solvent desalting, the main component is still observed only for Y element, proving the deposition of Y metal. It might be a coincidence the appearance of a pentagonal structure. However, these phenomena further support that the subsequently formed nuclei migrate to the previous circular nucleation sites (Fig. 10) to further form a fully covered compact film.

Moreover, the subsequent formed nuclei seem have a partiality for further growth on fresh tungsten surface in a 2D mode instead of a 3D growth on the previously formed Y nucleus until the final formation of a uniform and compressed film. Tang and Pesic reported that the formation of a very dense and thin film of Nd[3]and Er[37] on a Mo surface, primarily caused by the merge and overlapping of peripheric dendritic growth of the original nucleation sites. This overlapping leaded to a very high nuclei density of agglomerates promoting a very smooth and compact film surface. In our case, no distinct dendritic structure is seen on the W surface for the Y nucleation and growth, but the phenomenon of overlapping is still visible in Figs. 11d–11e. We can see, the nuclei density (areas A) between the dense sites (red dotted cycle areas) clearly is higher than that in periphery (areas B) of a single compact site. As proposed in previous studies et al.,[3,31,37] the phenomenon mode of initial formation of 3D nucleus and subsequent peripheric 2D growth is the cause of the deviation between experimental data and theoretical instantaneous nucleation mode as shown in Fig. 9.

To further obtain a perfect Y film, 60 s of deposition at a higher overpotential of −2.1 V vs Ag/AgCl was carried out on the tungsten disk electrode in LiCl-KCl-9.981 × 10^{-5} mol ml^{-1} YCl_3 melts. As presented in Figs. 13a, a sharp SEM image for the dense and uniform Y film is obtained. The element composition was also characterized by element mapping (Figs. 13b–13d) and EDS (Fig. 13e) analyses. The results confirm a very pure and compact Y film. A very small amount of salt was detected and primarily located at the regions with large nucleus size and rough areas as expected.

Conclusions

The diffusion coefficient, apparent standard potential and electrocrystallization of yttrium in LiCl-KCl eutectic are investigated by different electrochemical techniques such as CV, CP and OCP. The diffusion coefficients determined respectively by CP and CV methods at the temperature ranging from 673–823 K of two yttrium concentrations (YCl_3 = 3.816 × 10^{-5} mol ml^{-1} and 9.981 × 10^{-5} mol ml^{-1}) are in a range from 0.453 × 10^{-5} cm^2 s^{-1} to 8.25 × 10^{-5} cm^2 s^{-1} and provide the apparent activation energies range from 15.87 to 33.9 kJ mol^{-1}.

Based on the CA technique and Scharifker-Hill models, the theoretical mode of Y nucleation is confirmed to be instantaneous regardless the given temperature, over-potential and concentration.

With the application of W disk electrode and SEM-EDS techniques, the nucleation and initial growth of yttrium is visualized on the tungsten surface. Individual circular regions corresponding to the Y nucleation sites were firstly formed on the tungsten surface. Once a circular region formed, the continually formed nuclei migrate toward the initial circular nucleation sites to promote the following growth inside and peripheral of the circle. No dendritic structure for the Y deposition was observed on the W surface, but the overlapping of peripheric growth was still visualized to further form a very dense Y film. The visualization of yttrium nucleation and growth phenomena broadens the scope of Y electrochemistry on the W surface and is of practical significance for the electrochemical extraction and separation of lanthanides in preprocessing and the electrochemical preparation of thin Y films in molten salt for material science.

Acknowledgments

This work was financially supported by the National Postdoctoral Program for Innovative Talents (No. BX20180387) and the China Postdoctoral Science Foundation Grant (2019M653182), the National Natural Science Foundation of China (NSFC, No. 51904360 and

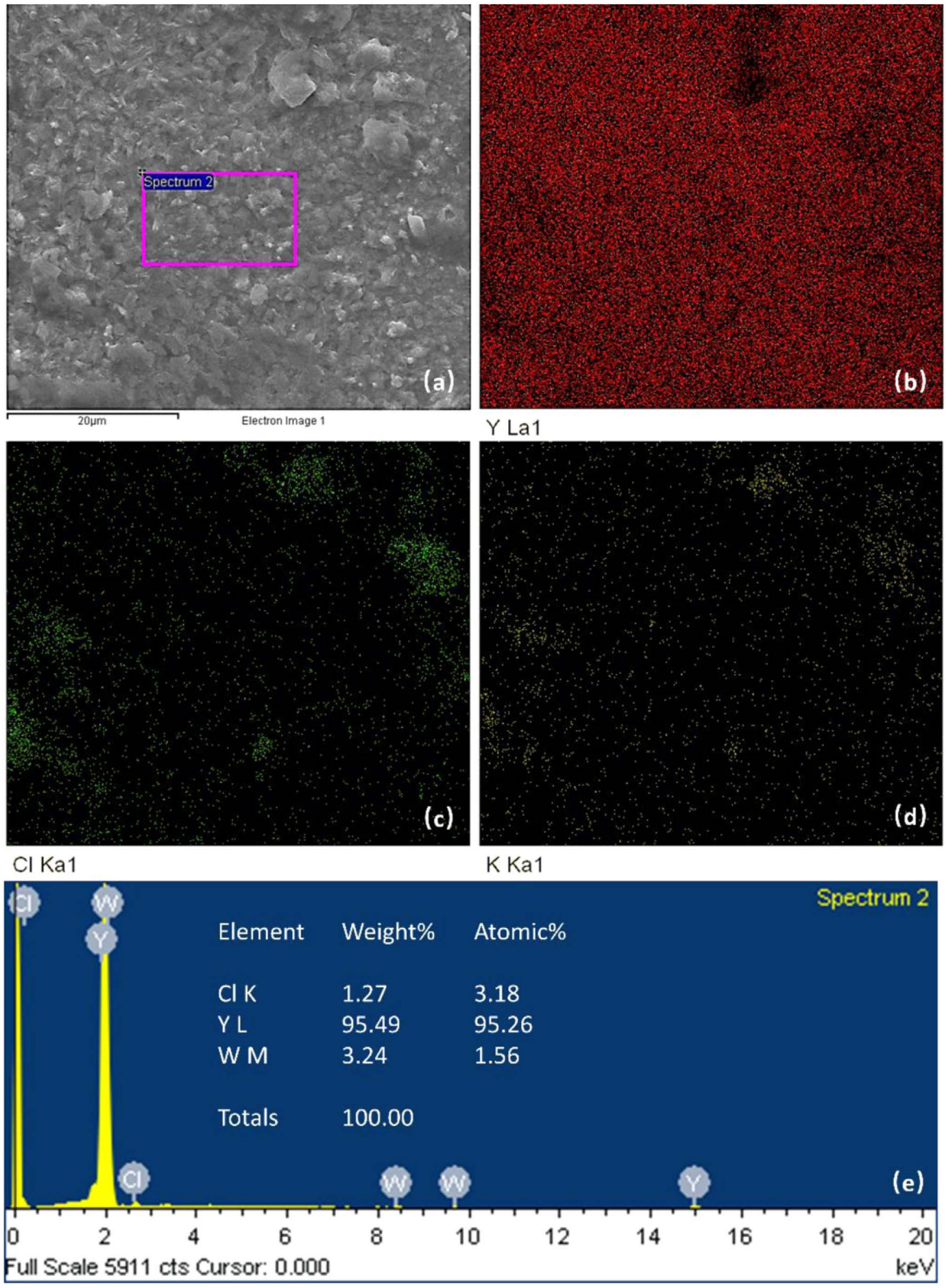

Figure 13. SEM images (a), element mapping analysis (b)–(d) and EDS (e) of Y film electrodeposited on tungsten disk surface at −2.1 V vs Ag/AgCl in LiCl-KCl-9.981 × 10^{-5} mol ml^{-1} YCl_3 melts for 60 s.

41773095) and the Fundamental Research Fund of Sun Yat-sen University (No. 191gpy293 and 45000-18833403).

ORCID

Kui Liu https://orcid.org/0000-0003-1454-2567

References

1. L. Borges Silverio and W. d. Q. Lamas, *Energy Policy*, **39**, 281 (2011).
2. Y. Castrillejo, M. Bermejo, A. Martínez, and A. P. Díaz, *J Min Metall B: Metall*, **39**, 109 (2003).
3. H. Tang and B. Pesic, *J. Nucl. Mater.*, **458**, 37 (2015).
4. J. N. Mathur, M. S. Murali, and K. L. Nash, *Solvent Extr. Ion Exch.*, **19**, 357 (2001).

5. V. A. Volkovich, T. R. Griffiths, and R. C. Thied, *J. Nucl. Mater.*, **323**, 49 (2003).
6. J. He, Z. Hua, H. Liu, L. Xu, S. He, Y. Yang, and Z. Zhao, *J. Electrochem. Soc.*, **165**, E598 (2018).
7. E.-H. Kim, G.-I. Park, Y.-Z. Cho, and H.-C. Yang, *Nucl. Technol.*, **162**, 208 (2008).
8. L. Yang and R. Hudson, *J Trans. Metall. Soc. AIME*, **215**, 589 (1959).
9. Y. Hoshino and J. A. Plambeck, *Can. J. Chem.*, **48**, 685 (1970).
10. Y. Sato and M. Hara, *Mater. Trans.*, **37**, 1525 (1996).
11. T. Hijikata, M. Sakata, H. Miyashiro, K. Kinoshita, T. Higashi, and T. Tamai, *Nucl. Technol.*, **115**, 114 (1996).
12. S. Hikino, G. Xie, K. Ema, Y. Ito, and Z. M. Shou, *J. Electrochem. Soc.*, **139**, 1820 (1992).
13. F. Lantelme, T. Cartailler, Y. Berghoute, and M. Hamdani, *J. Electrochem. Soc.*, **148**, C604 (2001).
14. I. Tolstobrov, O. El'kin, A. Bushuev, D. Kondrat'ev, and V. Kozvonin, *Rus Metal (Metally)*, **2018**, 777 (2018).
15. W. Han, W. Li, M. Li, Z. Li, Y. Sun, X. Yang, and M. Zhang, *J. Solid State Electrochem.*, **22**, 2435 (2018).
16. M. R. Shaltry, T.-S. Yoo, and G. L. Fredrickson, *Experimental Study of Codeposition Electrochemistry Using Mixtures of ScCl3 and YCl3 in LiCl-KCl Eutectic Salt at 500° C*, Idaho National Lab. (INL), Idaho Falls, ID (United States) (2017).
17. K. Liu, J. Sun, L. Zhu, Y. Sang, W. Shi, Z. Chai, B. Wang, and M. Kang, *J. Electrochem. Soc.*, **166**, D606 (2019).
18. K. Liu, Y. Ma, M. L. Kang, and B. Wang, *Electrochem. Commun.*, **117**, 106780 (2020).
19. T. Berzins and P. Delahay, *J. Am. Chem. Soc.*, **75**, 555 (1953).
20. J. Serp, P. Chamelot, S. Fourcaudot, R. Konings, R. Malmbeck, C. Pernel, J.-C. Poignet, J. Rebizant, and J.-P. J. E. A. Glatz, *Electrochim. Acta*, **51**, 4024 (2006).
21. J. Serp, R. Konings, R. Malmbeck, J. Rebizant, C. Scheppler, and J.-P. J. J. O. E. C. Glatz, *J. Electroanal. Chem.*, **561**, 143 (2004).
22. G. Y. Kim, D. Yoon, S. Paek, S. H. Kim, T. J. Kim, and D. H. Ahn, *J. Electroanal. Chem.*, **682**, 128 (2012).
23. I. Tolstobrov, O. El'kin, A. Kovalevskii, and V. Chebykin, *Rus Metal (Metally)*, **2015**, 626 (2015).
24. D. Yoon, S. Phongikaroon, and J. S. Zhang, *J. Electrochem. Soc.*, **163**, E97 (2016).
25. A. Bard, L. Faulkner, J. Leddy, and C. Zoski, *Electrochemical methods: fundamentals and applications* (Weily, New York) 2, 308 (1980).
26. Y. Wang, W. Zhou, and J. Zhang, *J. Nucl. Mater.*, **478**, 61 (2016).
27. S. Fusselman, J. Roy, D. Grimmett, L. Grantham, C. Krueger, C. Nabelek, T. Storvick, T. Inoue, T. Hijikata, and K. Kinoshita, *J. Electrochem. Soc.*, **146**, 2573 (1999).
28. J. Zhang, *J. Nucl. Mater.*, **447**, 271 (2014).
29. B. Scharifker and G. Hills, *Electrochim. Acta*, **28**, 879 (1983).
30. G. Gunawardena, G. Hills, I. Montenegro, and B. Scharifker, *J Electroanal Chem and Interf Electrochem*, **138**, 225 (1982).
31. H. Tang and B. Pesic, *Electrochim. Acta*, **119**, 120 (2014).
32. H. Tang, Y. Du, Y. Li, M. Wang, H. Wang, Z. Yang, B. Li, and R. Gao, *J. Nucl. Mater.*, **508**, 403 (2018).
33. Y. Castrillejo, M. Bermejo, A. Barrado, R. Pardo, E. Barrado, and A. Martinez, *Electrochim. Acta*, **50**, 2047 (2005).
34. A. Samin, Z. Wang, E. Lahti, M. Simpson, and J. Zhang, *J. Nucl. Mater.*, **475**, 149 (2016).
35. W. Zhou, J. Zhang, and Y. Wang, *J. Electrochem. Soc.*, **165**, E712 (2018).
36. A. Samin, A. Hastings, and J. Zhang, *J. Nucl. Mater.*, **467**, 628 (2015).
37. H. Tang and B. Pesic, *Electrochim. Acta*, **133**, 224 (2014).